Supporting information

Boosting Ultra-Fast Charging in Lithium Metal Batteries through Enhanced Solvent-Anion Interaction via Conjugation Effect

Jialin Wang[a, b#], Lin Xie[a, b#], Wanbao Wu[*a,c,d], Yihong Liang[a, b], Miaomiao Cao[a, b], Chaochao Gao[a, b], Yiyang Bo[a, b], Jichuan Zhang[a, b], Jiaheng Zhang[*a, b]

[a]*Sauvage Laboratory for Smart Materials, Harbin Institute of Technology (Shenzhen), 518055, China.*

E-mail: zhangjiaheng@hit.edu.cn; wuwanbao@stu.hit.edu.cn

[b]*School of Materials Science and Engineering, Harbin Institute of Technology (Shenzhen), 518055, China.*

[c]*School of Petrochemical Engineering, Changzhou University, 21300, China*

[d]*Changzhou Qianmu New Energy Co. Ltd., Changzhou, 21300, China*

Experimental section

Material preparation:

Lithium bis(fluorosulfonyl)imide (LiFSI), prop-1-ene-1,3-sultone (PES), and fluoroethylene carbonate (FEC) were procured from Tansoole Co., Ltd., (Shanghai, China), and utilized in their as-received state. LiFSI and PES were combined in precise molar ratios of 1:2 and 1:2.5, denoted as LPES2 and LPES2.5, respectively. This meticulous ratio control is imperative for fine-tuning electrolyte properties. These electrolyte mixtures were prepared at a controlled temperature of 60 °C and blended until achieving optically clear solutions, attesting to their purity and homogeneity enhance the electrochemical performance and stability. Next, 5 wt.% of FEC was introduced into LPES2.5, resulting in the creation of the electrolyte, hereafter referred to as DEE.[1] All electrolyte preparations were meticulously carried out inside an argon-filled glove box, with a monitored and maintained atmosphere containing less than 0.2 ppm of both H_2O and O_2. A carbonate electrolyte was prepared for comparative purposes, consisting of 1 M $LiPF_6$ (DoDoChem Co., Ltd., Suzhou, China) dissolved in a solvent with a precise 1:1:1 volume ratio of ethylene carbonate (EC), diethyl carbonate (DEC), and ethyl methyl carbonate (EMC), which is referred to as 'carbonate electrolytes' throughout the manuscript.

The cathodes consisted of $LiFeO_4$ (Canrd Co., Ltd., Guangdong, China), Super P (Canrd Co., Ltd., Guangdong, China), and polyvinylidene fluoride (PVDF) (Canrd Co., Ltd., Guangdong, China) in an 8:1:1 mass ratio. The powders were dispersed using N-methylpyrrolidone in an FA25 superfine homogenizer. A uniform film, 100 μm thick, was coated onto aluminum foil using the slurry coating method and dried at 60 °C for 6 hours. The dried electrodes were converted into 13 mm discs and further dried overnight in a vacuum oven at 80 °C.

Electrochemical measurements:

The LFP||Li coin cells were assembled in a controlled atmosphere in the standard 2032 format. DEE was accompanied by glass fiber separators and 120 μL of electrolyte, while carbonate electrolytes used polypropylene separators and 30 μL of electrolyte. Lithium metal foils with diameter of 15.8 mm, obtained from Canrd Co., Ltd., were

used as received. Charge and discharge tests were performed at room temperature using a NEWARE BTS-51 battery testing system. Galvanostatic cycling tests were performed within a voltage range of 2.5–4.2 V for the LFP electrodes in lithium-ion batteries (LIBs). Electrochemical impedance spectroscopy (EIS), linear sweep voltammetry (LSV), and cyclic voltammetry (CV) were performed using a CHI 760E electrochemical workstation.

Characterizations:

To measure the viscosity of the deep eutectic electrolytes (DEEs), we employed SV-1A viscometer sourced from A&D Co., Ltd., Tokyo, Japan for room temperature testing and MCR72 rheometer sourced from Anton Paar Ltd., China for low temperature testing. NMR spectrometer (Bruker BioSpin GmbH, Billerica, USA) with a pulsed-field gradient probe was used for the measurements. ^{1}H, ^{7}Li, and ^{19}F NMR spectra were recorded for PES, Li$^+$, and FSI$^-$, respectively. The ionic conductivities of the DEEs were determined at a stable temperature of 25 °C, utilizing a precision conductivity meter (308F, Leici Co., Ltd., Shanghai, China). A Raman spectrometer (LabRAM Hr800, Horida, USA) was used to capture the Raman spectra. The morphology of the Li anode and LFP cathode after undergoing 50, 100, 200 cycles within the LFP‖Li cells was characterized using a field emission scanning electron microscope (SEM, HITACHI SU8010, Japan). We used X-ray photoelectron spectroscopy (XPS) to identify the chemical composition of the lithium anode surface after cycling.

Theoretical simulations:

Our approach involved all-atom molecular dynamic (MD) simulations using GROMACS 2020.3.[2] The topological parameters of all molecules were separately generated using Sobtop.[3] The atomic charges of all the molecules were assigned to RESP charges using the Multiwfn program.[4] The simulation boxes (size of 50 Å × 50 Å × 50 Å) were filled randomly with 100 Li$^+$, 100 FSI$^-$, and 250 PES/PS molecules using PACKMOL.[5] System temperature was maintained at 298 K throughout the simulation. We initiated the process with energy minimization by utilizing the steepest descent method until a termination gradient of 100 was reached. A time step of 2 fs was

employed to ensure temporal precision, and equilibration of the system was achieved via a 2 ns NPT run, followed by 1 ns NVT runs at 298 K. The total simulation time was 100 ns, with the final 50 ns designated for structural characterization of the electrolyte. Visual representation of the molecular structures and snapshots of MD structures were facilitated using visual molecular dynamics (VMD 1.9.3).[6]

The structural optimization and electrostatic potentials of the molecules were calculated using DFT at the B3LYP/6-311G+(d,p) level with a D3 dispersion correction for weak interaction energies to ensure comprehensive accuracy.[7-9] The energies of the combined molecules and wave function were evaluated at the B3LYP-D3(BJ)/ma-TZVP(-f) level. All DFT calculations were conducted using the Gaussian 16 software package. Further analytical insights encompassed reduced density gradient analyses, electrostatic potential mapping, topological analysis, weak interactions in chemical systems, interaction region indicator calculations, and bond critical points (BCPs) of each interaction.[10-12] These analytical tasks were executed using Multiwfn and VMD, providing a deeper understanding of the electrostatic and chemical phenomena in the system.
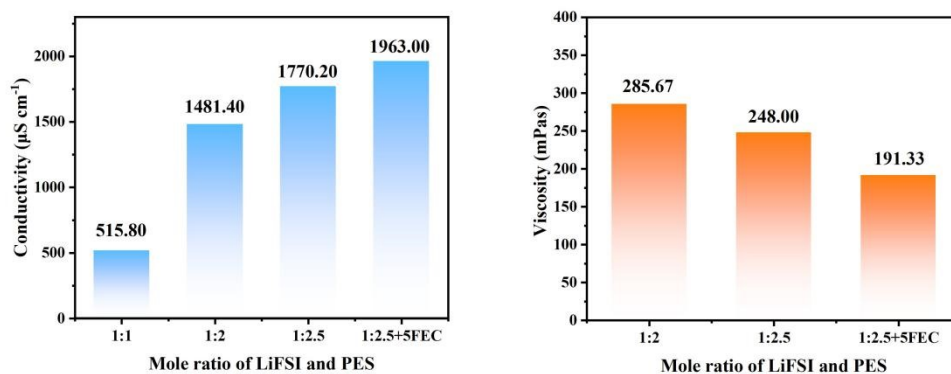
Fig. S1 The ionic conductivity **a)** and viscosity **b)** of different electrolytes at 25 °C.
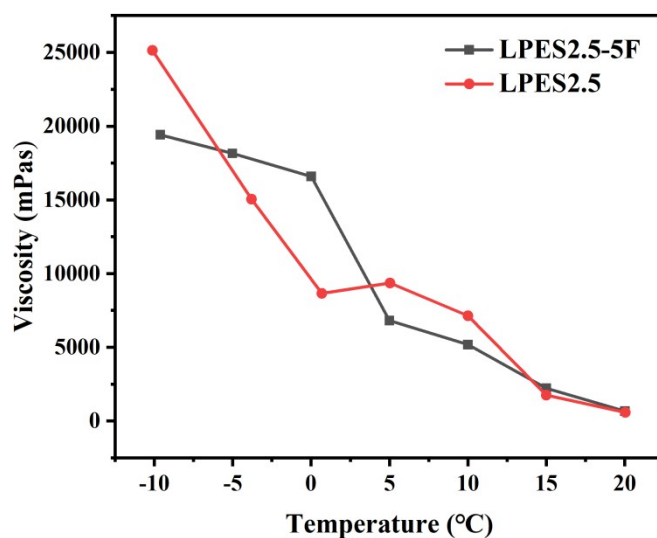

Fig. S2 The viscosity of LPES2.5-5F and LPES2.5 at different temperature.

As shown in Fig. S2, LPES2.5 remained in a liquid state even at -10 ℃, albeit with a significantly higher viscosity of 25141 mPas compared to that at 25 ℃. Furthermore, after added 5 wt.% FEC to LPES2.5 (referred to as LPES2.5-5F), the resulting electrolyte exhibited a lower viscosity at -10 ℃ (19408 mPas) compared to LPES2.5 alone.
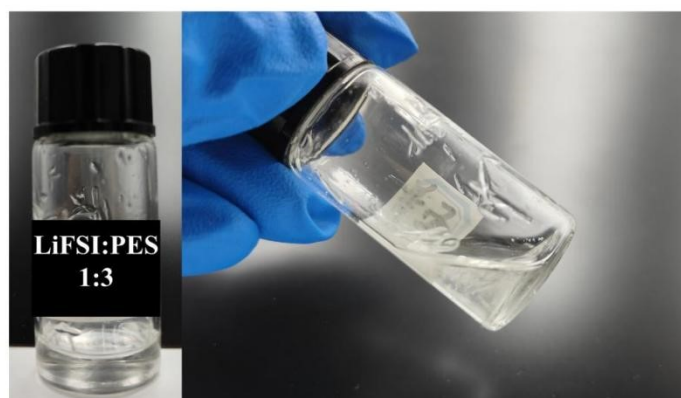
Fig. S3 Photos of the LiFSI:PES electrolyte using a molar ratio of 1:3.
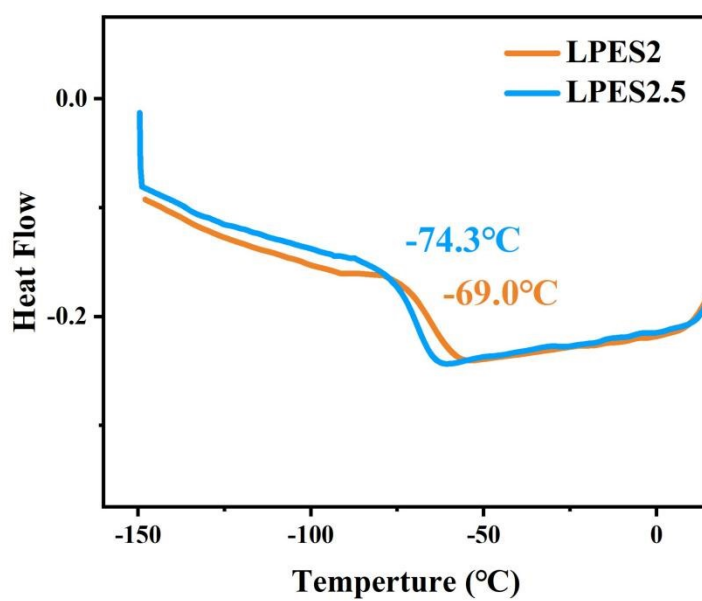
Fig. S4 Differential scanning calorimetry analysis of LPES2 and LPES2.5.
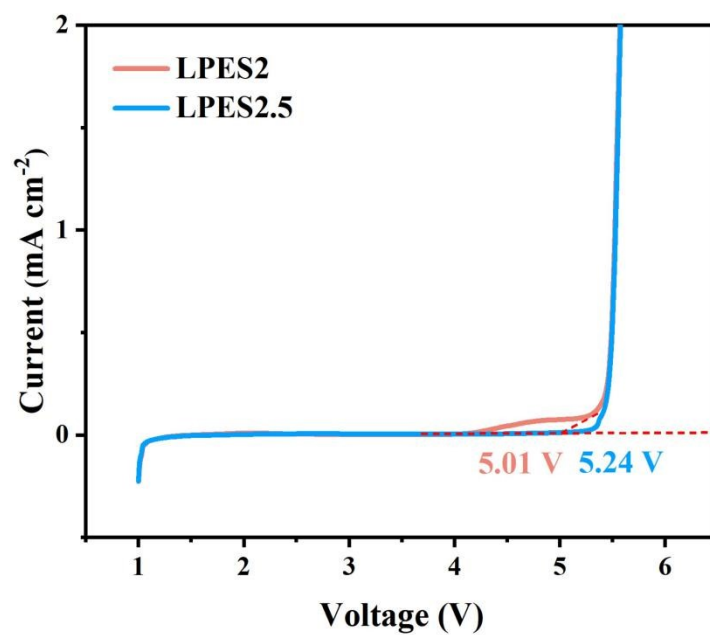
Fig. S5 LSV of LPES2 and LPES2.5 in the cells with an SS working electrode and a Li film as the counter electrodes.
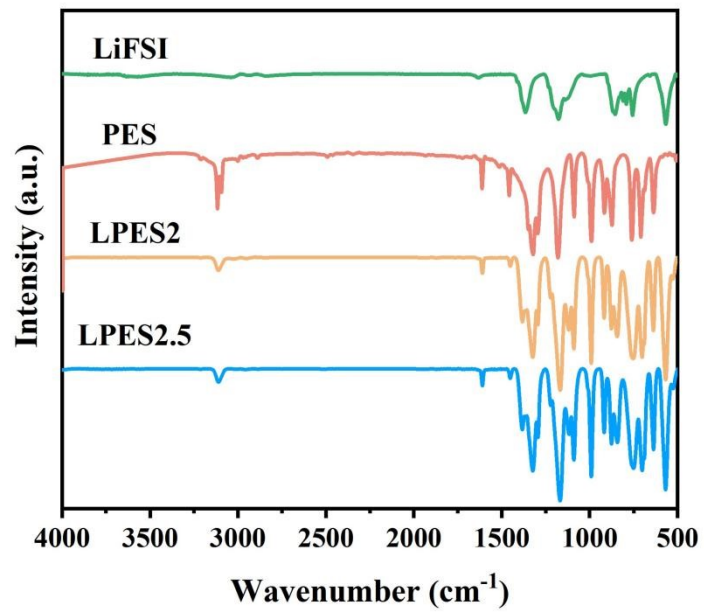
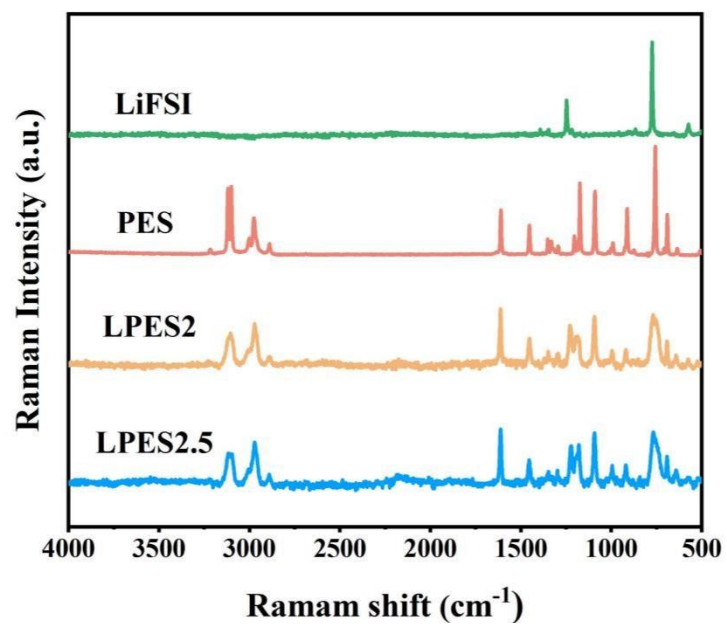**Fig. S6** FTIR spectra of LiFSI, PES, LPES2, and LPES2.5.

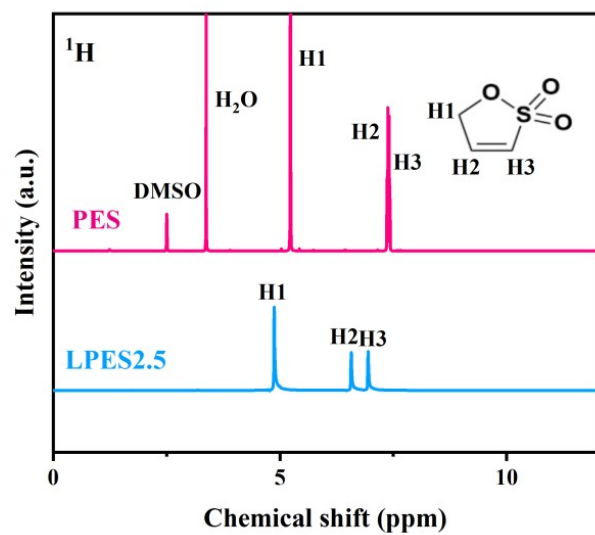**Fig. S7** Raman spectra of LiFSI, PES, LPES2, and LPES2.5.
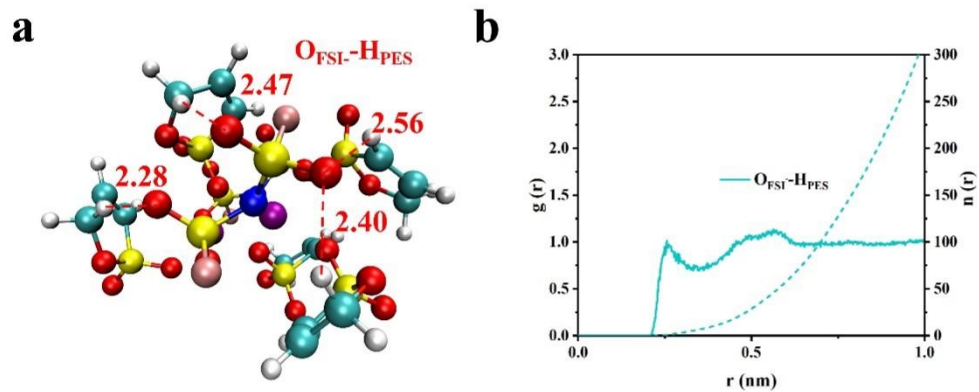
Fig. S8 ^{1}H NMR spectra of PES and LPES2.5

Fig. S9 (a) DFT geometry optimization analysis of LPES2.5. (b) RDF of $O_{FSI}-H_{PES}$ in LPES2.5 calculated from MD simulation. (Li in purple, N in blue, O in red, C in cyan, H in white, S in yellow, and F in pink).
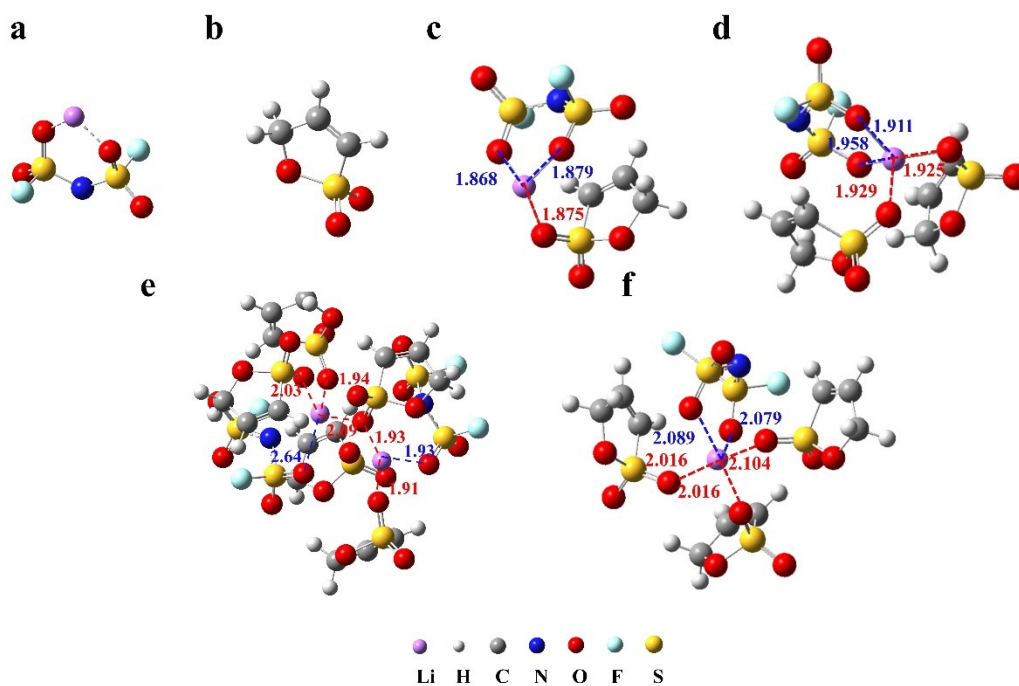
Fig. S10 DFT geometry optimization of **(a)** LiFSI, **(b)** PES, **(c)** LiFSI-1PES, **(d)** LiFSI-2PES, **(e)** LiFSI-2.5PES, and **(f)** LiFSI-3PES (Li in purple, N in blue, O in red, C in cyan, H in white, S in yellow, and F in ochre).
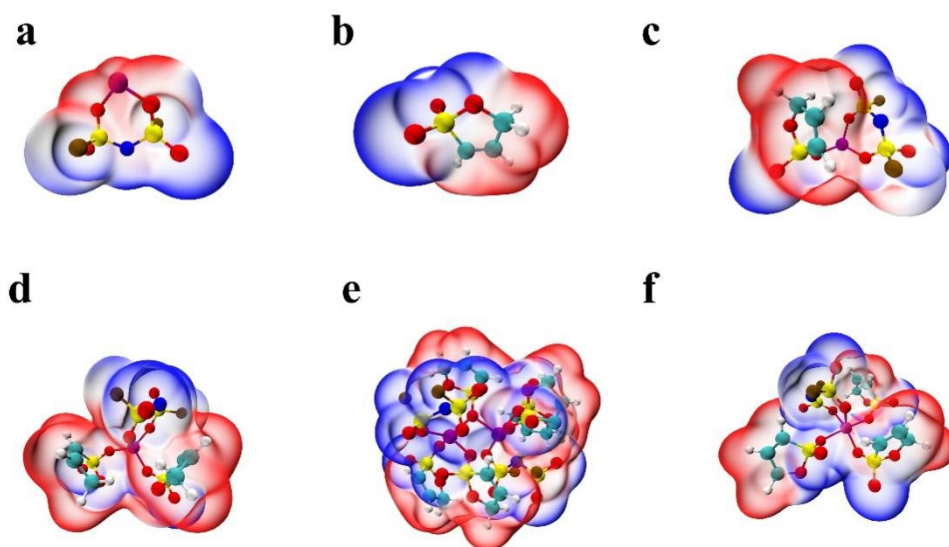
Fig. S11 Molecular electrostatic potential energy surfaces of **(a)** LiFSI, **(b)** PES, **(c)** LiFSI-1PES, **(d)** LiFSI-2PES, **(e)** LiFSI-2.5PES, and **(f)** LiFSI-3PES (Li in purple, N in blue, O in red, C in cyan, H in white, S in yellow, and F in ochre).
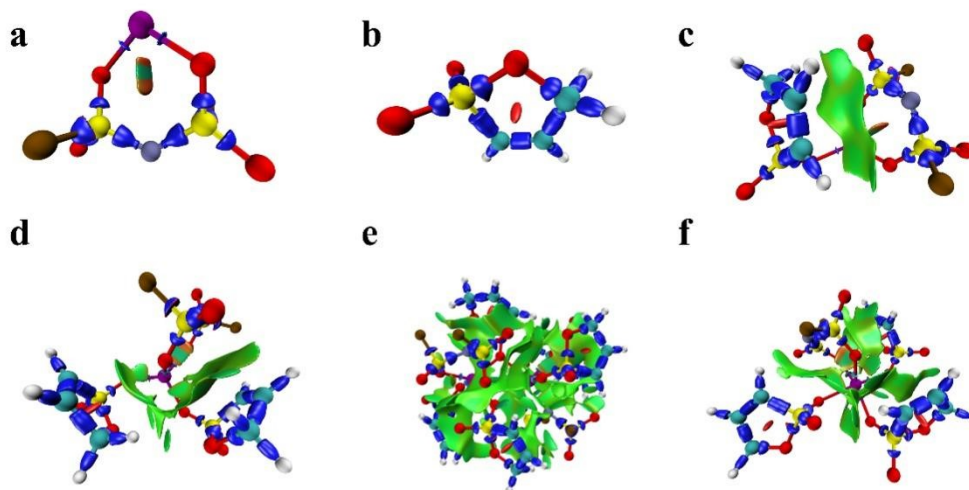
Fig. S12 Isosurface map of IRI of four systems of **(a)** LiFSI, **(b)** PES, **(c)** LiFSI-1PES, **(d)** LiFSI-2PES, **(e)** LiFSI-2.5PES, and **(f)** LiFSI-3PES (Li in purple, N in ice blue, O in red, C in cyan, H in white, S in yellow, and F in ochre).
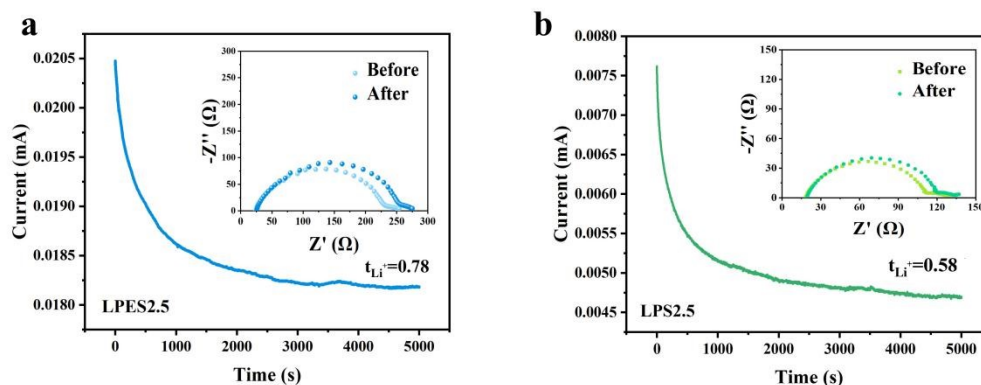
Fig. S13 Constant potential polarization potential curves and EIS spectra of (**a**) LPES2.5 and (**b**) LPS2.5 before and after polarization.
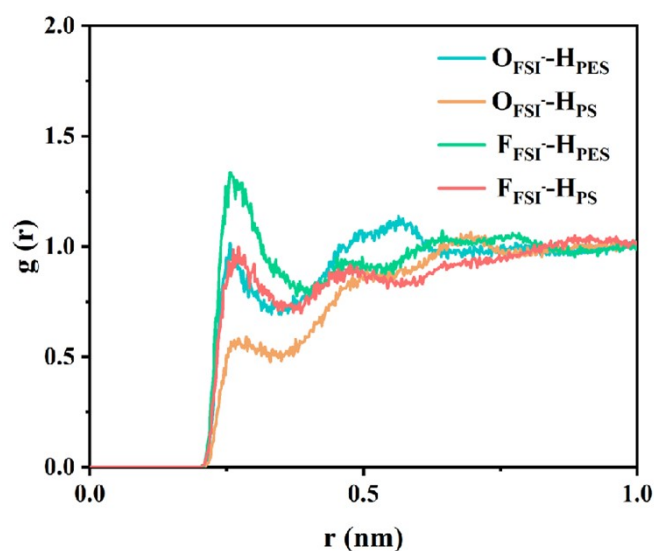

Fig. S14 RDF of different ion pairs in LPES2.5 and LPS2.5 calculated from MD simulation.

From the RDF of the simulation in Fig. S14, the peak at 2.5 Å can be obvious observed, corresponding to F_{FSI}–H_{PES} interactions. In contrast, the peak intensity between FSI$^-$ and PS appears to be weaker. This result suggests that the interaction between FSI$^-$ and PES is stronger than that between FSI$^-$ and PS.
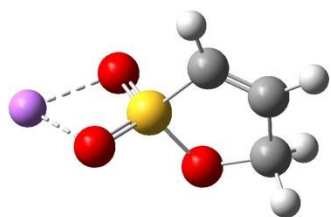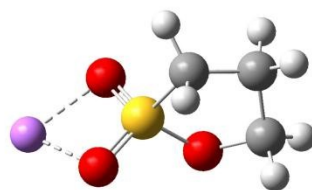
a

BE $_{PES-Li^+}$ = - 57.26 kcal/mol

b

BE $_{PS-Li^+}$ = - 58.04 kcal/mol

Fig. S15 Binding energy of (**a**) PES-Li$^+$ and (**b**) PS-Li$^+$ calculated from DFT simulation.
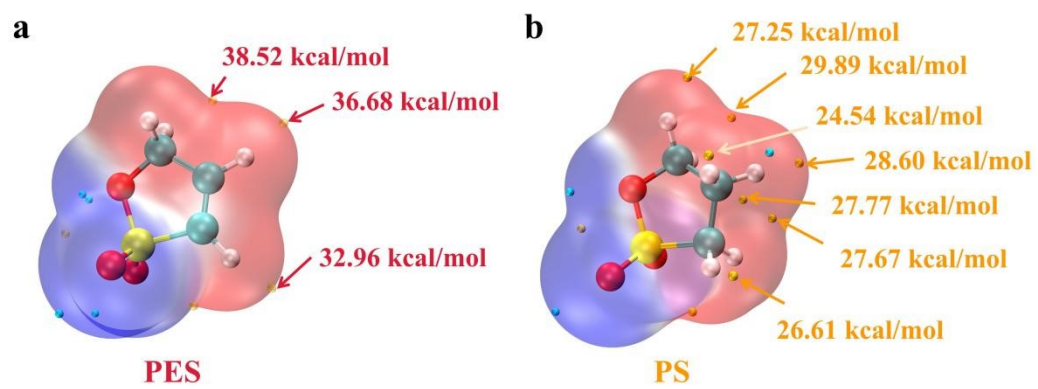
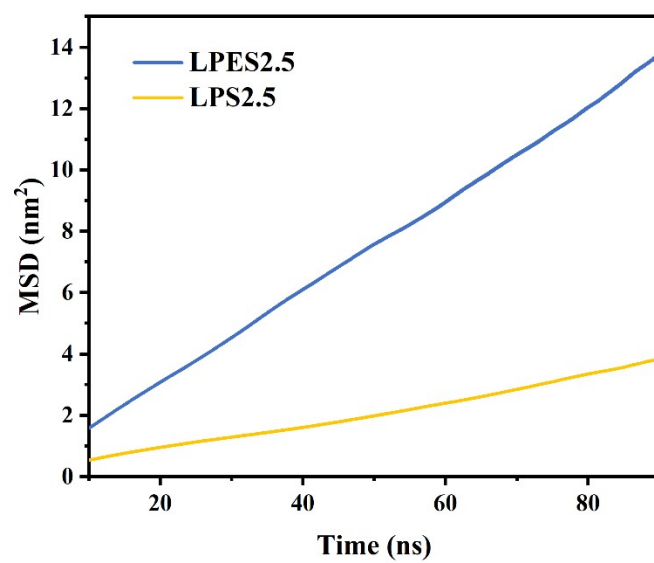**Fig. S16** Electrostatic potential analysis of PES and PS.

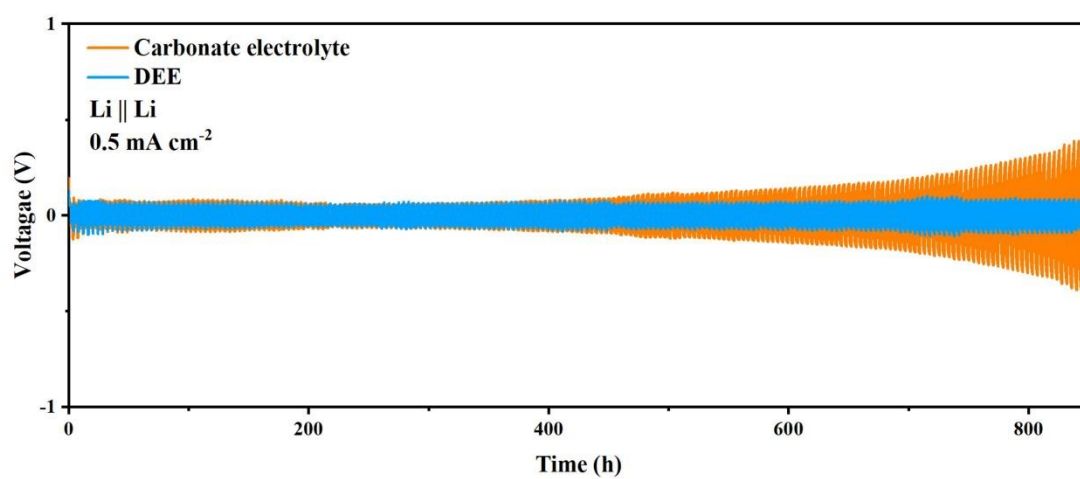**Fig. S17** MSD plot of Li$^+$ in LPES2.5 and LPS2.5.

Fig. S18 Galvanostatic cycling performance of Li‖Li symmetric cells with LPES2.5 and carbonate electrolytes at 0.5 mA cm⁻².
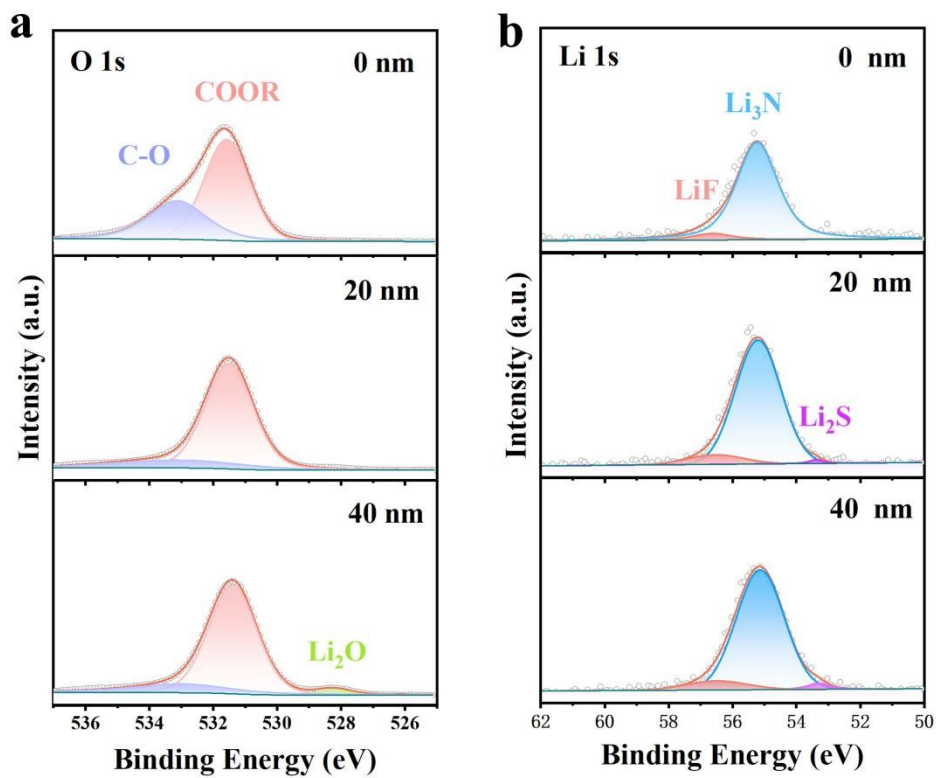
Fig. S19 XPS spectra of O 1s and Li 1s in cycled Li metal anodes of LFP‖DEE‖ Li batteries after 10 cycles.
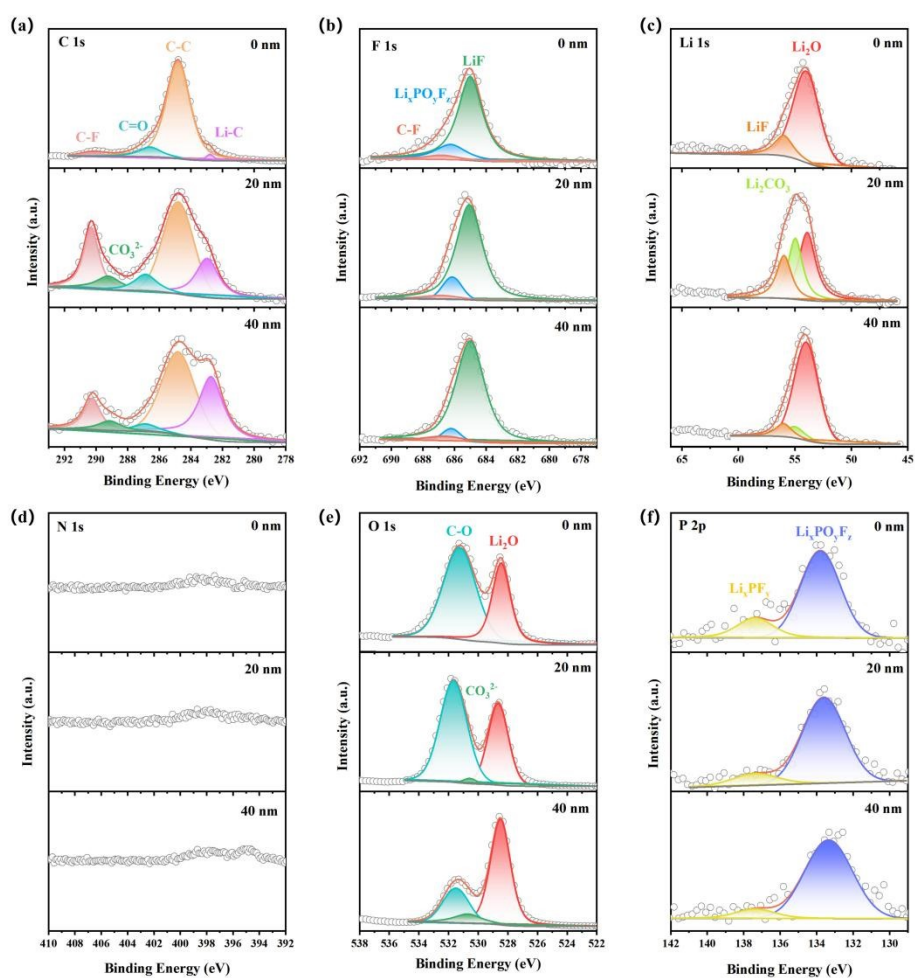
Fig. S20 XPS spectra of C 1s, F 1s, Li 1s, N 1s, O 1s and P 2p in LFP‖Li cells with carbonate electrolytes after 10 cycles.
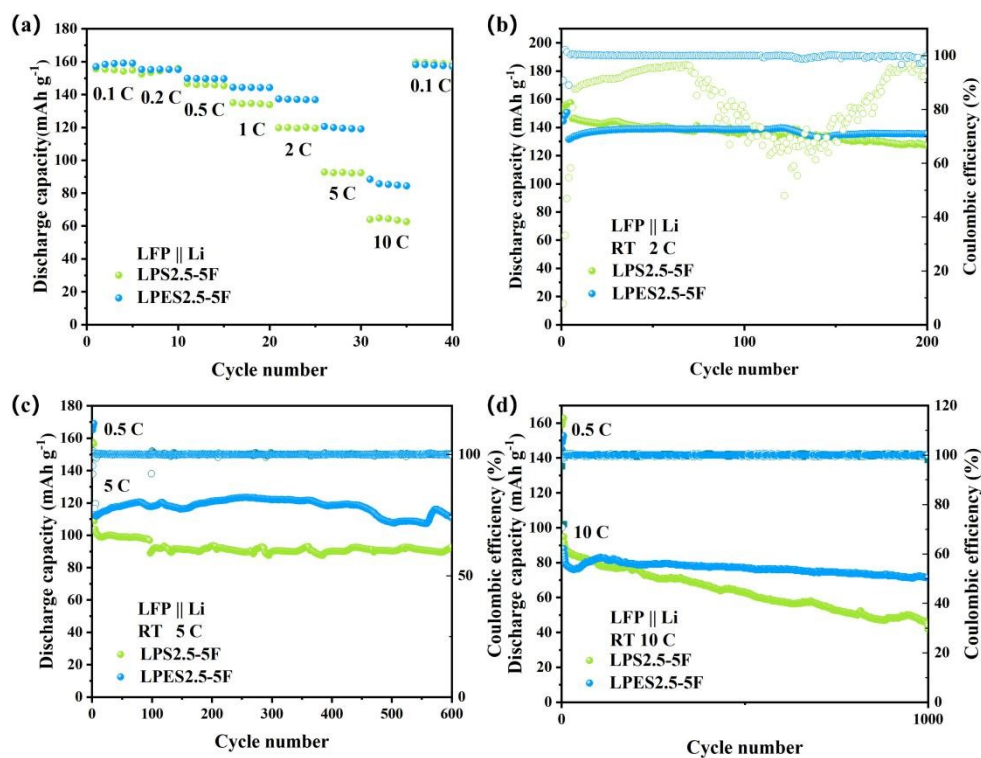
Fig. S21 Cycling performance comparison of LFP||Li cells utilizing LPES2.5 and LPS2.5 at 25 °C. (a) Rate performance of LFP||Li cells. Cycle performance of LFP||Li cells at (b) 2 C, (c) 5 C and (d) 10 C.

The electrochemical performance data for both LPS2.5 and LPES2.5 electrolyte systems have supplemented in Fig. S21. These results clearly show that LPES2.5 outperforms LPS2.5 in terms of both rate performance and long-cycle stability, which could confirm the effect of conjugation on electrochemical performance. Specifically, at 10 C, LPES2.5 retains 81.32% of its initial capacity after 1000 cycles, compared to only 45.70% for LPS2.5.

Fig. S22 Cycling performance of LFP||Li cells with different electrolytes at 25 °C and 2 C.
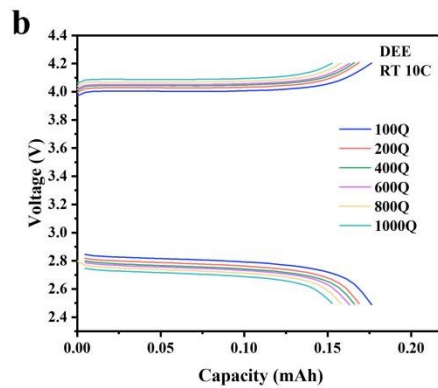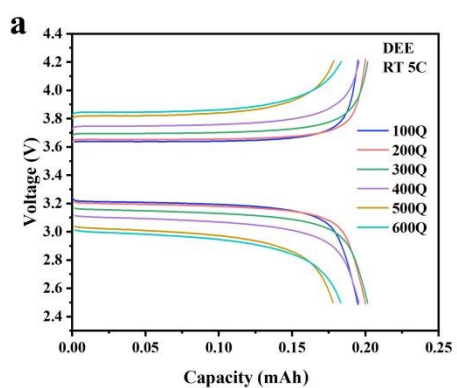
Fig. S23 Charge/discharge voltage profiles of LFP‖Li cells with LPES2.5 at different current densities at 25 °C.
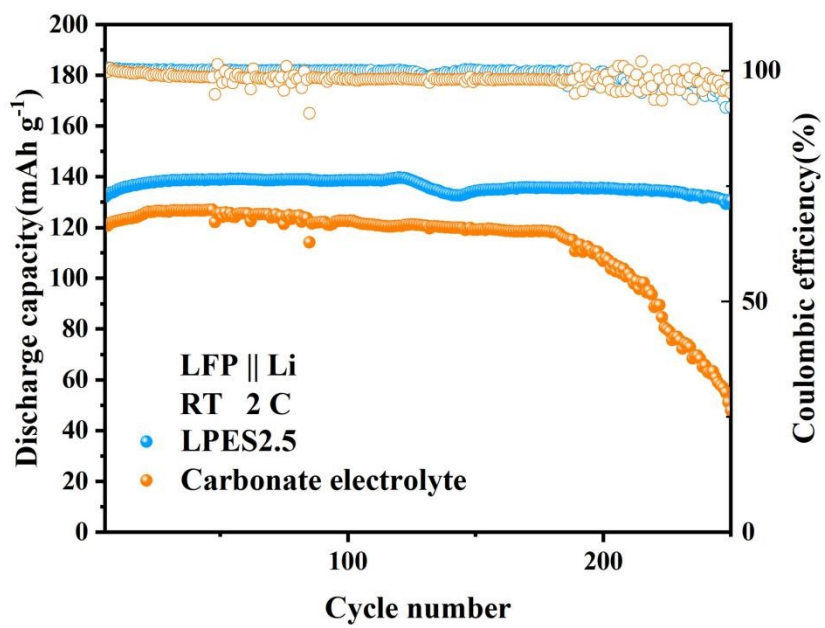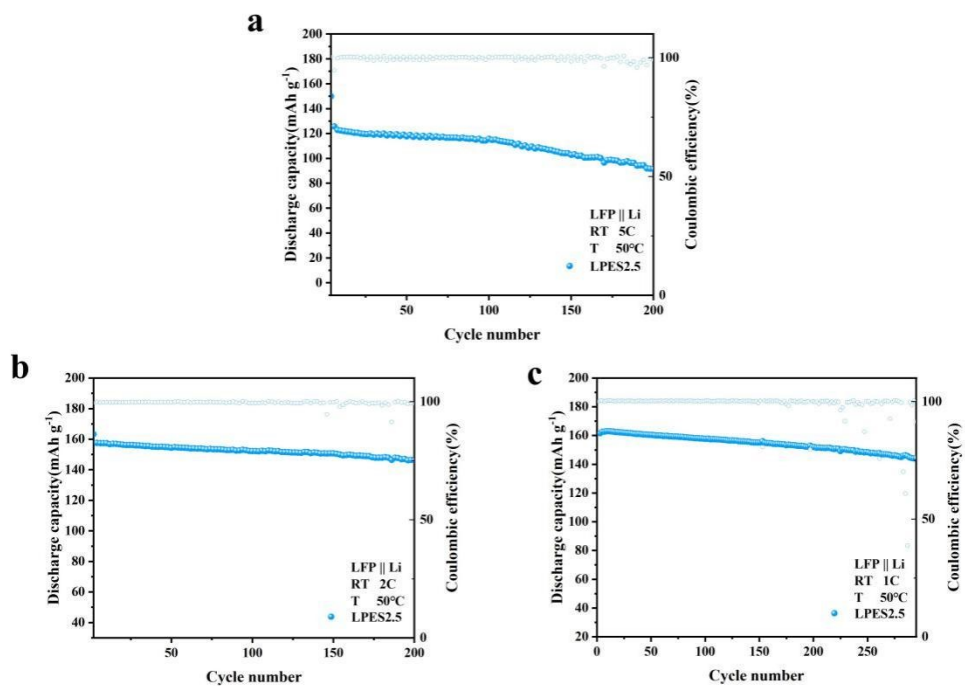
Fig. S24 Cycling performance of LFP‖Li cells with LPES2.5 at current densities of (**a**) 5 C, (**b**) 2 C, and (**c**) 1 C at 50 °C.
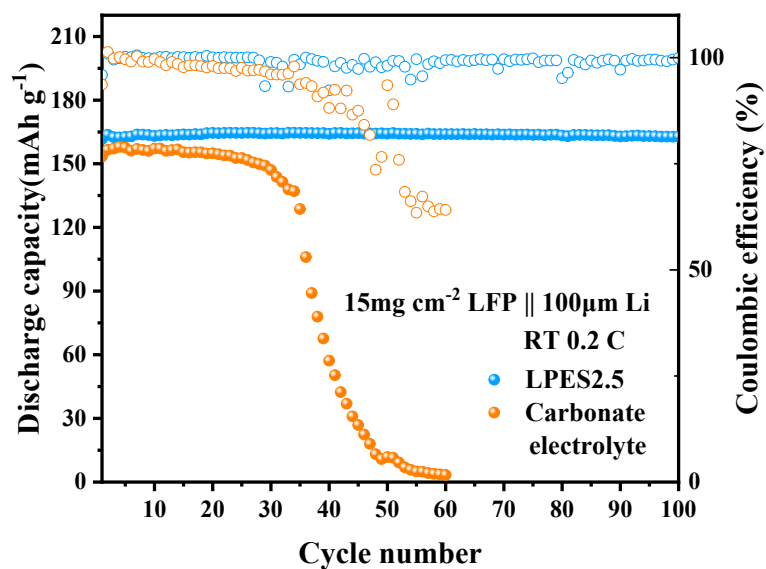
Fig. S25 Cycle performance of LFP‖Li cells with a highly loaded LFP electrode (15 mg cm⁻²) and thin Li cathode (100 μm).

Thick LFP cathodes with a high loading of approximately 15 mg cm^{-2} and a 100 μm lithium metal anode was applied in a full cell. (Fig. S25) When LPES2.5 is used as the electrolyte, the cell demonstrates satisfactory performance, with a capacity retention of 98.91% after 100 cycles at 0.2 C. In contrast, the cell with the carbonate electrolyte sustains performance up to 40 cycles before experiencing a drastic capacity drop.
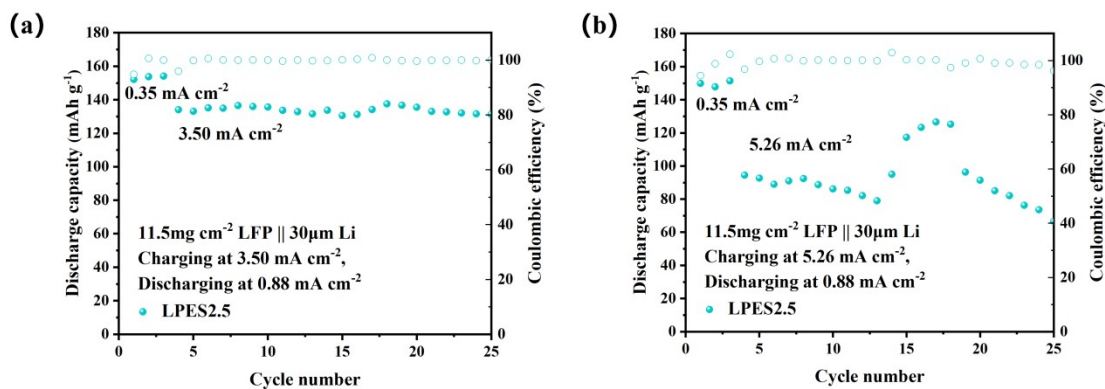
Fig. S26 Cycle performance of LFP‖Li cells with a high loading LFP cathode (11.5 mg cm^{-2}) and thin Li anode (30 μm) at (a) 3.50 mA cm^{-2} (2 C) and (b) 5.26 mA cm^{-2} (3 C).
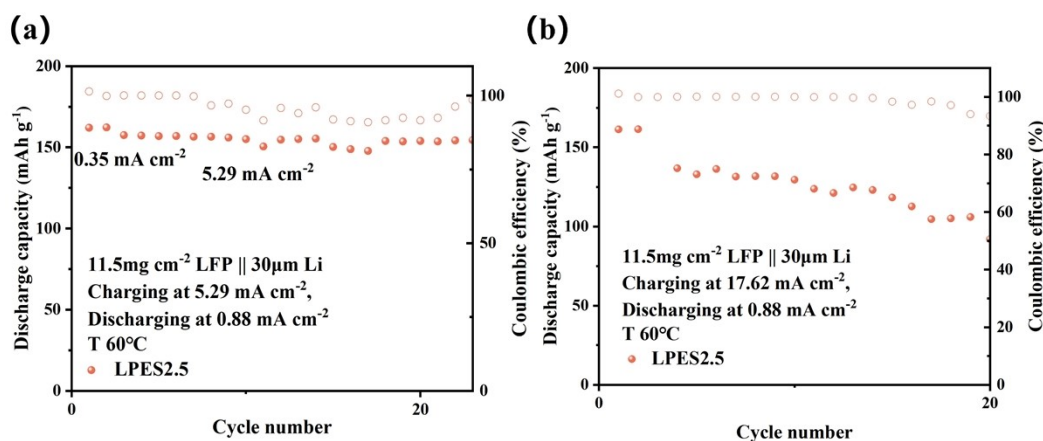
Fig. S27 Cycle performance of LFP‖Li cells with a high loading LFP cathode (11.5 mg cm^{-2}) and thin Li anode (30 μm) at (a) 5.29 mA cm^{-2} (3 C) and (b) 17.62 mA cm^{-2} (10 C) at 60 °C.

The full cell with a high loading LFP cathode and a 30 μm Li metal was used to assess the cycling performance at high current densities (Fig. S26). At a current density of 5.26 mA cm^{-2} (3 C), LPES2.5 as the electrolyte was able to cycle properly with an average Coulombic efficiency of 99.58% over 20 cycles. Furthermore, at an elevated temperature of 60 °C, the viscosity of LPES2.5 decreases. The cell with LPES2.5 exhibited an initial capacity of 132.99 mAh g^{-1} with an average Coulombic efficiency of 99.40% over 15 cycles at current densities up to 17.62 mA cm^{-2} (10 C) (Fig. S27).
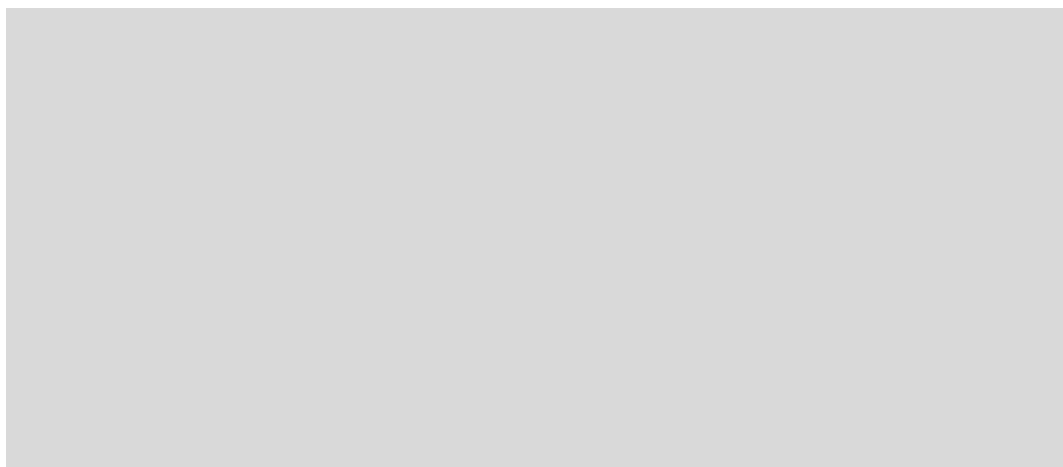
Fig. S28 Cycle performance of LFP‖Li cells with a highly loaded LFP electrode (15 mg cm^{-2}) and thin Li cathode (30 μm) at (a) 0.235 mA cm^{-2} (0.1 C)and (c) 4.695 mA cm^{-2}(2 C).

To meet the requirements for practical use, a battery with a 15 mg cm^{-2} thick LFP cathode and a 30 μm thick Li metal anode was assembled, achieving an N/P ratio of 2.5 (Fig. S28). At 0.235 mA cm^{-2}(0.1 C), the initial capacities of the battery using LPES2.5 as the electrolyte were 169.21 mAh g^{-1}. The capacity of the battery showed negligible decay after 30 cycles. Notably, under conditions of charging at 4.695 mA cm^{-2} (2 C) and discharging at 1.17 mA cm^{-2}(0.5 C), LPES2.5 still maintained stable cycle performance.
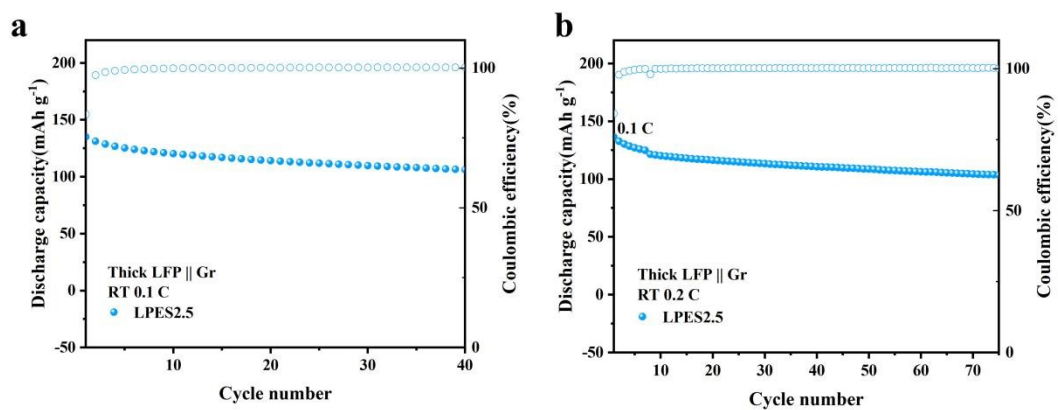
Fig. S29 Cycling performance of LFP||Gr cells with LPES2.5 at 0.1 C **(a)** and 0.2 C **(b)** at 25 °C.
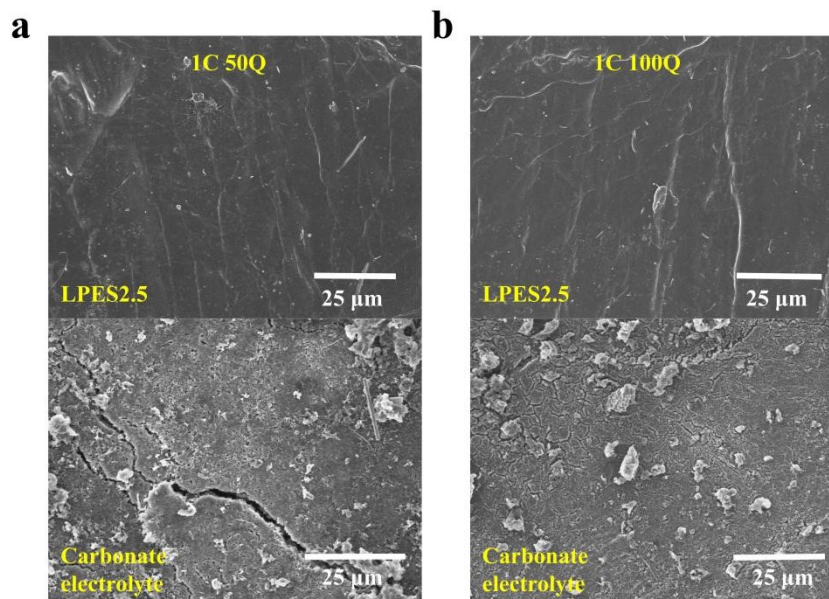
Fig. S30 SEM images of lithium metal after **(a)** 50 cycles and **(b)** 100 cycles of LFP||Li cells with LPES2.5 (top) and carbonate electrolytes (bottom).
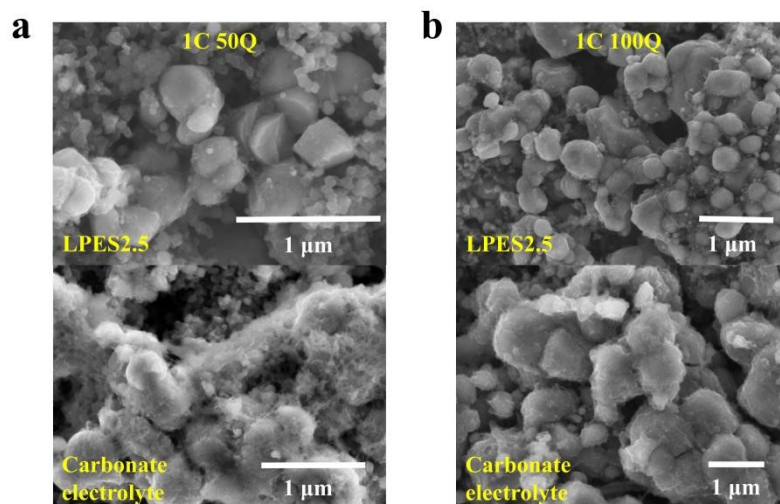
Fig. S31 SEM images of LFP cathode after **(a)** 50 cycles and **(b)** 100 cycles of LFP‖Li cells with LPES2.5 (top) and carbonate electrolytes (bottom).
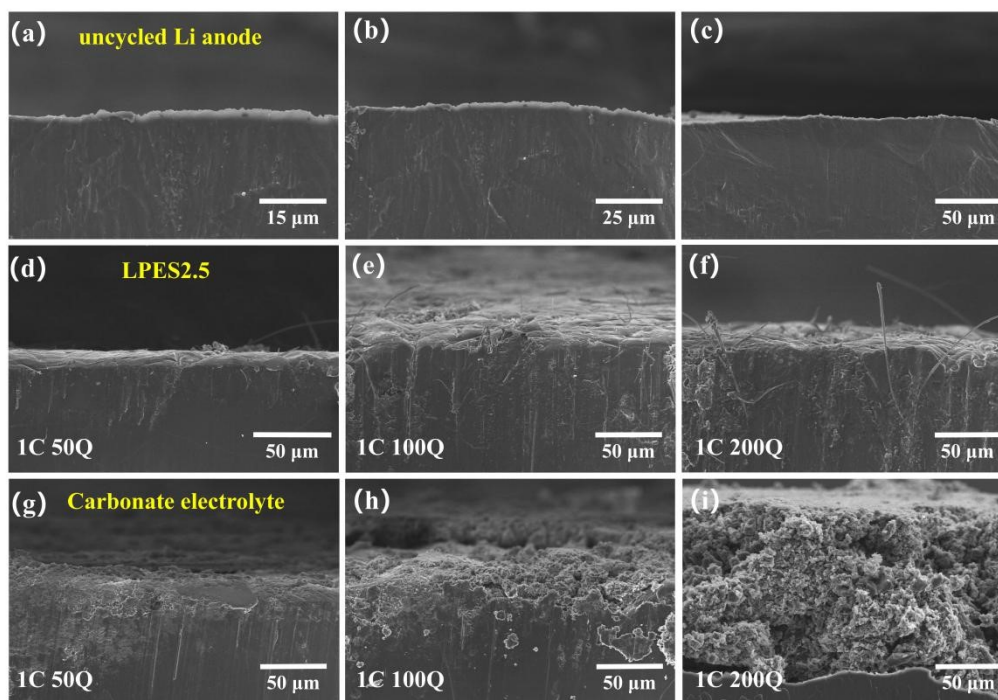
Fig. S32 (a-c) SEM images of uncycled Li anode. Comparative SEM images depicting the cross-section of lithium metal after 50, 100 and 200 cycles of LFP‖Li cells using (d-f) LPES2.5 and (g-i) carbonate electrolytes.
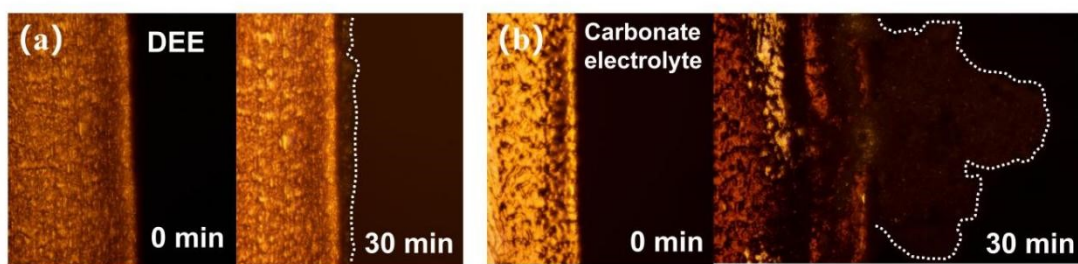
Figure. S33 Deposition morphology of the Li deposited on Cu foils using in situ optical microscopy in Li‖Cu cells with (a) LPES2.5 and (b) carbonate electrolytes at a current density of 0.5 mA cm^{-2}.

Table S1 Number and density of molecules in the simulation box.

	LPES2.5	LPS2.5
LiFSI	100	100
PES	250	250
Density (g/cm^3)	1.550	1.529

Table S2 The coordination number.

	LPES2.5	LPS2.5
O_{FSI^-} (within 2.80 of Li)	2.979	3.333
$O_{PES/PS}$ (within 2.80 of Li)	2.370	2.081
H_{PES} (within 2.80 of O_{FSI^-})	2.144	-

Table S3 Lithium transfer number (t_{Li+}) in different types of electrolytes.

	Electrolyte Composition	t_{Li+}	Ref.
DEE	Pylacrylamide+LiTFSI	0.36	[13]
	DSM-SPE	0.56	[14]
	LiTVI+PEGMA+PC	0.52	[15]
	LiTFSI+NML +PEGDA + UPyMA	0.66	[16]
	DMMSA-LiTFSI	0.33–0.4	[17]
	SL-LiTFSI	0.47	[18]
	DMIm-LiTFSI	0.65	[19]
IL	1:1 mol/mol Li[TFSA]-[C3C1pyrr][FSA]	0.201	[20]
	1:2 mol/mol Li[TFSA]-[C3C1pyrr][FSA]	0.098	[20]
	1:10 mol/mol Li[TFSA]-[C3C1pyrr][FSA]	0.037	[20]
	PDADMATFSI-Li[TFSI]-[EMIM][TFSI]	0.41	[21]
	[EMIM][TFSI]+UIO-67+PVDF-HFP+LiTFSI	0.45	[22]
	Polymeric imidazolium-based ionic liquid+[DEIM][TFSI+LiTFSI]	0.26	[23]
	PDEIm+PVDF-HFP+LiTFSI	0.42	[24]
	[PP13][TFSI]+PVDF-HFP+LITFSI	0.59	[25]
	[S2][TFSI]+PEO+LiTFSI	0.31	[26]
	EMIM][TFSI]+PVDF-HFP+LAGP+LITFSI	0.54	[27]
	[EMIM][TFSI]+PEO+LiTFSI	0.39	[28]
HCE	3.25 mol dm^{-3} LiFSI in SL	0.58	[29]
	4 mol dm^{-3} LiTFSI in DME	0.5–0.6	[30]
	4 mol dm^{-3} LiClO4 in DOL/DME (1:1, v/v)	0.46	[31]
	4 mol dm^{-3} LiTFSI in DOL/DME (1:1, v/v)	0.67	[31]
	4 mol dm^{-3} LiFTFSI in DOL/DME (1:1, v/v)	0.68	[31]
	0.52:1:0.09 mol/mol/mol LiFSI-AN–VC	0.57	[32]
	1:1.5 mol/mol LiTFSA-GN	0.74	[33]
	7 mol dm^{-3} LiTFSI in DOL/DME (1:1, v/v)	0.73	[34]

Table S4. Discharge capacity values of floating test cell.

Electrode materials	Test hours [h]	Fresh cell capacity [mAh g^{-1}]	After test capacity [mAh g^{-1}]	Capacity retention [%]
LPES2.5	24	154.64	154.58	99.96%
	72	152.48	150.43	98.66%
	120	155.26	153.12	98.62%
	168	154.01	153.83	99.88%
	240	154.14	146.85	95.27%
Carbonate electrolyte	24	150.33	142.63	94.88%
	72	147.24	128.34	87.16%
	120	144.27	91.87	63.68%
	168	147.68	71.07	48.12%
	240	151.39	57.39	37.91%

References:

1. H. Zhao, X. Yu, J. Li, B. Li, H. Shao, L. Li and Y. Deng, *Journal of Materials Chemistry A*, 2019, **7**, 8700-8722.
2. M. J. Abraham, T. Murtola, R. Schulz, S. Páll, J. C. Smith, B. Hess and E. Lindahl, 2015, **1-2**.
3. T. Lu, Sobtop, Version, http://sobereva.com/soft/Sobtop).
4. T. Lu and F. Chen, *Journal of Computational Chemistry*, 2012, **33**, 580-592.
5. L. Martínez, R. Andrade, E. G. Birgin and J. M. Martínez, *Journal of Computational Chemistry*, 2009, **30**, 2157-2164.
6. W. Humphrey, A. Dalke and K. Schulten, *Journal of Molecular Graphics*, 1996, **14**, 33-38.
7. A. D. Becke, *The Journal of Chemical Physics*, 1993, **98**, 5648-5652.
8. S. Grimme, J. Antony, S. Ehrlich and H. Krieg, *The Journal of Chemical Physics*, 2010, **132**, 154104.
9. S. Grimme, L. Ehrlich S Fau - Goerigk and L. Goerigk.
10. T. Lu and Q. Chen, in *Comprehensive Computational Chemistry (First Edition)*, eds. M. Yáñez and R. J. Boyd, Elsevier, Oxford, 2024, DOI: https://doi.org/10.1016/B978-0-12-821978-2.00076-3, pp. 240-264.
11. D. Cremer and E. Kraka, *Angewandte Chemie International Edition in English*, 1984, **23**, 627-628.
12. R. Bianchi, G. Gervasio and D. Marabello, *Inorganic Chemistry*, 2000, **39**, 2360-2366.
13. C. Zhang, Z. Niu, J. Bae, L. Zhang, Y. Zhao and G. Yu, *Energy & Environmental Science*, 2021, **14**, 931-939.
14. C. Wang, T. Wang, L. Wang, Z. Hu, Z. Cui, J. Li, S. Dong, X. Zhou and G. Cui, *Advanced Science*, 2019, **6**.
15. J.-H. Baik, S. Kim, D. G. Hong and J.-C. Lee, *ACS Applied Materials & Interfaces*, 2019, **11**, 29718-29724.
16. H. Wang, J. Song, K. Zhang, Q. Fang, Y. Zuo, T. Yang, Y. Yang, C. Gao, X. Wang, Q. Pang and D. Xia, *Energy & Environmental Science*, 2022, **15**, 5149-5158.
17. O. E. Geiculescu, D. D. DesMarteau, S. E. Creager, O. Haik, D. Hirshberg, Y. Shilina, E. Zinigrad, M. D. Levi, D. Aurbach and I. C. Halalay, *Journal of Power Sources*, 2016, **307**, 519-525.
18. G. Chen, Y. Zhang, C. Zhang, W. Ye, J. Wang and Z. Xue, *ChemSusChem*, 2022, **15**.
19. X. Pei, Y. Li, T. Ou, X. Liang, Y. Yang, E. Jia, Y. Tan and S. Guo, *Angewandte Chemie International Edition*, 2022, **61**.
20. H. Zhang, W. Qu, N. Chen, Y. Huang, L. Li, F. Wu and R. Chen, *Electrochimica Acta*, 2018, **285**, 78-85.
21. M. Safa, A. Chamaani, N. Chawla and B. El-Zahab, *Electrochimica Acta*, 2016, **213**, 587-593.
22. L. Liu and C. Sun, *ChemElectroChem*, 2020, **7**, 707-715.
23. P. Guo, A. Su, Y. Wei, X. Liu, Y. Li, F. Guo, J. Li, Z. Hu and J. Sun, *ACS Applied Materials & Interfaces*, 2019, **11**, 19413-19420.
24. Z. Hu, J. Chen, Y. Guo, J. Zhu, X. Qu, W. Niu and X. Liu, *Journal of Membrane Science*, 2020, **599**, 117827.
25. X. Pan, T. Liu, D. J. Kautz, L. Mu, C. Tian, T. E. Long, P. Yang and F. Lin, *Journal of Power Sources*, 2018, **403**, 127-136.

26.   M. D. Widstrom, K. B. Ludwig, J. E. Matthews, A. Jarry, M. Erdi, A. V. Cresce, G. Rubloff and P. Kofinas, *Electrochimica Acta*, 2020, **345**, 136156.

27.   Q. Guo, Y. Han, H. Wang, S. Xiong, W. Sun, C. Zheng and K. Xie, *The Journal of Physical Chemistry C*, 2018, **122**, 10334-10342.

28.   L. Balo, Shalu, H. Gupta, V. Kumar Singh and R. Kumar Singh, *Electrochimica Acta*, 2017, **230**, 123-131.

29.   J. Alvarado, M. A. Schroeder, M. Zhang, O. Borodin, E. Gobrogge, M. Olguin, M. S. Ding, M. Gobet, S. Greenbaum, Y. S. Meng and K. Xu, *Materials Today*, 2018, **21**, 341-353.

30.   J. Qian, W. A. Henderson, W. Xu, P. Bhattacharya, M. Engelhard, O. Borodin and J.-G. Zhang, *Nature Communications*, 2015, **6**.

31.   Q. Ma, Z. Fang, P. Liu, J. Ma, X. Qi, W. Feng, J. Nie, Y. S. Hu, H. Li, X. Huang, L. Chen and Z. Zhou, *ChemElectroChem*, 2016, **3**, 531-536.

32.   Z. Peng, X. Cao, P. Gao, H. Jia, X. Ren, S. Roy, Z. Li, Y. Zhu, W. Xie, D. Liu, Q. Li, D. Wang, W. Xu and J. G. Zhang, *Advanced Functional Materials*, 2020, **30**.

33.   Y. Ugata, R. Tatara, K. Ueno, K. Dokko and M. Watanabe, *The Journal of Chemical Physics*, 2020, **152**.

34.   L. Suo, Y.-S. Hu, H. Li, M. Armand and L. Chen, *Nature Communications*, 2013, **4**.